ChemComm

ROYAL SOCIETY OF CHEMISTRY

COMMUNICATION

View Article Online
View Journal

Cite this: DOI: 10.1039/d5cc03568f

Received 24th June 2025,
Accepted 22nd July 2025

DOI: 10.1039/d5cc03568f

rsc.li/chemcomm

Two-dimensional porphyrin-based covalent organic frameworks for visible-light-driven oxidative coupling of benzylamines†

Qing-Ru Zhao,[a] Kui Wang,[b] Xiaokai Gao[a] and Chunyan Tan *[ab]

Two porphyrin-based covalent organic frameworks (COFs), Por-bpy-COF and Por-Pd/bpy-COF, were developed as visible-light-responsive photocatalysts. Featuring broad light absorption ($\lambda >$ 400 nm) and a palladium center in Por-Pd/bpy-COF for enhanced charge separation, both achieved >97% conversion of benzylamine to imine under visible light and ambient oxygen in 1 hour. Post-reaction analyses showed high structural stability, with Por-Pd/bpy-COF retaining >95% catalytic activity over five cycles, offering a sustainable strategy for green synthesis.

Visible-light photocatalysis enables sustainable organic synthesis under mild conditions by activation of inert bonds while reducing the use of toxic reagents and energy consumption.[1,2] However, designing efficient photocatalysts with recyclability remains challenging. Homogeneous transition metal complexes (*e.g.*, Ru/Ir) suffer from deactivation/recovery issues,[3,4] while inorganic semiconductors (*e.g.*, TiO_2) lack visible-light absorption ($\lambda >$ 400 nm) and exhibit poor substrate affinity.[5,6] Thus, robust heterogeneous alternatives combining broad-spectrum absorption with precise active sites are essential for green chemistry applications.

Heterogeneous catalysts play a pivotal role in sustainable chemistry, with porous materials offering distinct advantages in recyclability and functionalization.[7] Covalent organic frameworks (COFs), as crystalline porous platforms, enable precise integration of light-harvesting units and catalytic sites through tunable dynamic covalent chemistry.[8,9] Their extended π-conjugation promotes directional charge separation, while ordered pores facilitate substrate diffusion and active site accessibility,[10] features critical for green catalytic cycles. Although explored for gas adsorption,[11,12] CO_2 reduction,[13,14] and catalysis,[15,16] their potential in photocatalytic organic transformations requiring precise spatial/electronic control remains underexploited.

Photocatalytic oxidative coupling of benzylamines to imines exemplified a key benchmark reaction for pharmaceutical/fine chemical synthesis, yet current methods often rely on noble/rare-earth metals, harsh conditions, or lack efficiency/selectivity.[17–19] While porphyrin-based COFs exhibit strong visible-light absorption,[20–23] their specific application in porphyrin COFs for sustainable imine synthesis has rarely been reported.

Herein, we report two recyclable two-dimensional (2D) porphyrin-based COFs (Por-bpy-COF and Por-Pd/bpy-COF) for photocatalytic oxidative coupling of benzylamines. This design enables efficient visible-light-driven aerobic oxidative coupling of benzylamines, establishing a sustainable heterogeneous photocatalysis platform aligned with green chemistry principles.

Two porphyrin-based covalent organic frameworks (COFs), namely Por-bpy-COF and Por-Pd/bpy-COF, were synthesized *via* solvothermal condensation of tetrakis(4-aminophenyl)-porphyrin with respective dialdehyde monomers ([2,2′-bipyridine]-5,5′-dicarboxaldehyde for the Por-bpy-COF; Pd-coordinated analogue for the Por-Pd/bpy-COF) (Scheme 1). The metal-free Por-bpy-COF and Pd-incorporated Por-Pd/bpy-COF were isolated in 74.7% and 78.4% yields, respectively, demonstrating the robustness of this synthetic approach for metalloporphyrin COFs.

FTIR spectroscopy confirmed the formation of imine bonds in both COFs (Fig. 1a). The characteristic C=N stretching vibrations at 1622 cm^{-1} (Por-bpy-COF) and 1624 cm^{-1} (Por-Pd/bpy-COF) exhibited a negligible 2 cm^{-1} shift, indicating minimal electronic perturbation upon Pd coordination. This conclusion is further corroborated by solid-state ^{13}C CP/MAS NMR spectra (Fig. S1 and S2, ESI†), where the imine carbonyl resonance at 160 ppm and the absence of residual aldehyde signals (~190 ppm) confirm complete condensation. The aromatic carbon signals (120–140 ppm) from porphyrin and bipyridine units remained intact in both COFs, verifying structural preservation during synthesis. Notably, the Por-Pd/bpy-COF displayed a distinct

[a] The State Key Laboratory of Chemical Oncogenomics, Institute of Biopharmaceutical and Health Engineering, Shenzhen International Graduate School, Tsinghua University, Shenzhen, 518055, P. R. China. E-mail: tancy@sz.tsinghua.edu.cn

[b] Open FIESTA, Shenzhen International Graduate School, Tsinghua University, Shenzhen 518055, P. R. China

† Electronic supplementary information (ESI) available: Experimental details including materials, synthesis, and instrumentation and some supplementary figures. See DOI: https://doi.org/10.1039/d5cc03568f

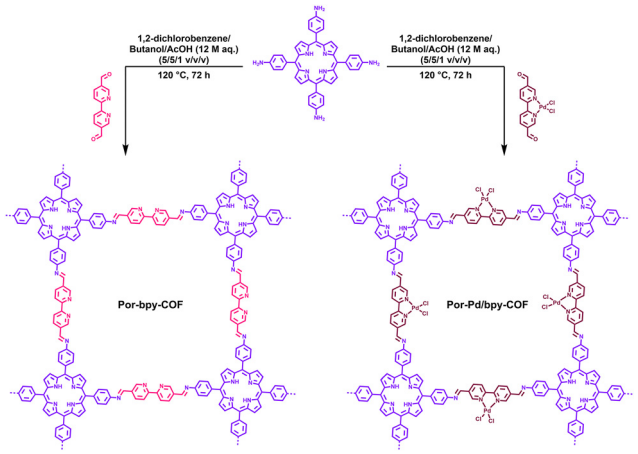

Scheme 1 Synthesis of the Por-bpy-COF and Por-Pd/bpy-COF.

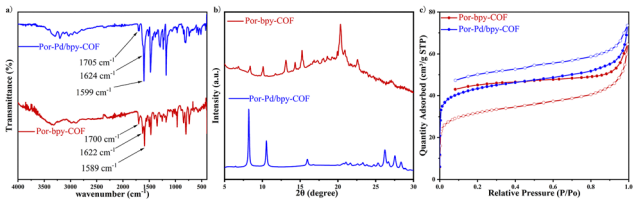

Fig. 1 Structural and compositional analysis of the Por-bpy-COF and the Por-Pd/bpy-COF. (a) Fourier-transform infrared (FTIR) spectra of the Por-bpy-COF and the Por-Pd/bpy-COF. (b) PXRD of the Por-bpy-COF and the Por-Pd/bpy-COF. (c) Nitrogen adsorption–desorption isotherms of the Por-bpy-COF and the Por-Pd/bpy-COF at 77 K.

deshielded peak at 150 ppm, attributable to Pd-induced electron density redistribution at the coordinated bipyridine carbons. Thermogravimetric analysis (TGA) revealed decomposition onset temperatures of 480 °C (Por-bpy-COF) and 320 °C (Por-Pd/bpy-COF) (Fig. S3, ESI†), with lower thermal stability of the latter likely arising from Pd-mediated framework destabilization at elevated temperatures.

PXRD analysis confirmed the long-range crystallinity of both COFs, with sharp low-angle reflections (Fig. 1b) characteristic of layered 2D architectures. Le Bail refinement yielded unit cell parameters of a = 29.7 Å, b = 30.2 Å, c = 4.39 Å for the Por-bpy-COF and a = 29.7 Å, b = 29.6 Å, c = 4.74 Å for the Por-Pd/bpy-COF. The expanded c-axis (Δc = +0.35 Å) in the Por-Pd/bpy-COF suggests that Pd coordination induces interlayer spacing enlargement, possibly through the steric effects of Pd centers or modified π–π interactions. Refinement residuals (R_{wp}/R_p = 5.44%/3.91% for the Por-bpy-COF *vs.* 7.60%/4.25% for the Por-Pd/bpy-COF) indicate localized structural disorder in the metalated COF, consistent with crystallinity challenges common to metal–organic hybrids.

Nitrogen sorption analysis at 77 K unveiled distinct porosity profiles for the two COFs, with the Por-Pd/bpy-COF exhibiting a 35% higher BET surface area (163 $m^2\ g^{-1}$) compared to the Por-bpy-COF (118 $m^2\ g^{-1}$) (Fig. 1c). The low experimental surface areas might be attributed to partial framework interpenetration and residual solvent molecules obstructing the nanochannels during activation. Remarkably, the Por-Pd/bpy-COF's superior surface area and preserved porosity—rarely achieved in metalated COFs—arise from Pd(II) coordination reinforcing structural rigidity, as evidenced by its negligible pore collapse during degassing. The optimized mesopore architecture (2–5 nm) synergistically facilitates substrate accessibility and charge confinement, enabling efficient photon-to-chemical conversion by accelerating mass transport while suppressing exciton recombination—a dual advantage critical for photocatalytic performance.

SEM imaging revealed spherical aggregates (200–500 nm diameter) for the Por-bpy-COF (Fig. 2a), indicative of isotropic growth under kinetic control, while the Por-Pd/bpy-COF formed lamellar microcrystals (1–2 μm lateral size) with well-defined edges (Fig. 2b), demonstrating Pd-directed anisotropic crystallization. This result is as expected, with the smaller surface area of the Por-bpy-COF in the form of small spheres, consistent with the previous results, and the Por-Pd/bpy-COF being able to form more crystals. High-resolution TEM showed an interlayer spacing of 0.35 nm for the Por-Pd/bpy-COF (Fig. 2d), consistent with its lamellar architecture. The discrepancy with the result obtained from the PXRD refinement result of 4.74 Å for the c-axis may be due to TEM projection artifacts (*e.g.*, tilted crystallites) and local stacking defects unresolved by bulk-sensitive XRD.

The optoelectronic properties of the synthesized COFs (Por-bpy-COF and Por-Pd/bpy-COF) were systematically investigated to elucidate their photocatalytic mechanisms. UV-vis diffuse reflectance spectroscopy (DRS) revealed broad absorption spanning 200–550 nm for both COFs (Fig. 3a), consistent with visible-light-harvesting capabilities. Tauc plot analysis derived from Kubelka–Munk transformations yielded optical bandgaps of 1.79 eV for the Por-bpy-COF and 2.10 eV for the Por-Pd/bpy-COF (Fig. 3b). The 0.31 eV bandgap enhancement upon Pd incorporation is attributed to metal-to-ligand charge transfer (MLCT) effects, where Pd-centered electrons populate antibonding π*-orbitals of the bipyridine ligand, raising the LUMO energy level. Mott–Schottky measurements at 1 kHz (Fig. S4, ESI†) confirmed n-type semiconductor behaviour for both

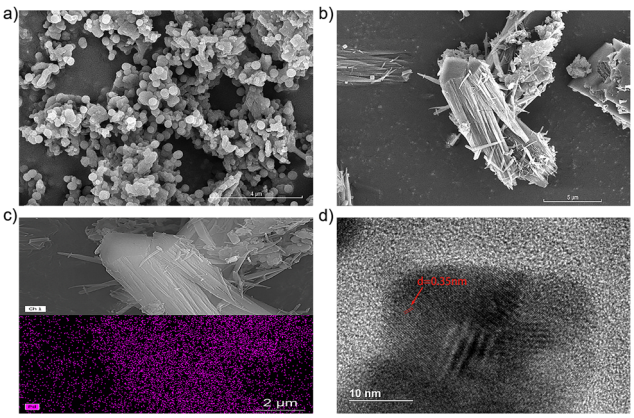

Fig. 2 Morphological and microstructural characterization of the Por-bpy-COF and the Por-Pd/bpy-COF. (a) SEM image of the Por-bpy-COF. (b) SEM image of the Por-Pd/bpy-COF. (c) EDS image of the Por-Pd/bpy-COF. (d) HR-TEM image of the Por-Pd/bpy-COF.

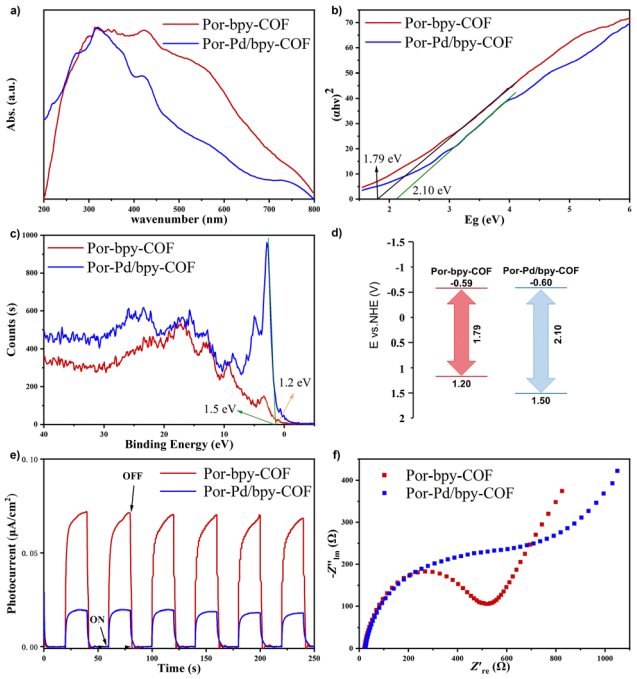

Fig. 3 Optoelectronic and electrochemical characterizations of the Por-bpy-COF and the Por-Pd/bpy-COF. (a) UV-vis diffuse reflectance spectra. (b) Tauc plots derived from DRS data for bandgap determination. (c) XPS valence band spectrum. (d) Energy band structures. (e) Photocurrent. (f) EIS of the Por-bpy-COF and the Por-Pd/bpy-COF.

COFs, as evidenced by positive slopes of $1/C^2$ *vs.* potential plots. XPS valence band spectra positioned the highest occupied molecular orbital (HOMO) levels at 1.20 V and 1.50 V *vs.* NHE for the Por-bpy-COF and the Por-Pd/bpy-COF, respectively (Fig. 3c). Combined with their bandgaps, their corresponding lowest unoccupied molecular orbital (LUMO) levels were calculated as $E_{LUMO} = E_{HOMO} + E_g$, yielding −0.59 V (Por-bpy-COF) and −0.60 V *vs.* NHE (Por-Pd/bpy-COF). These values provide sufficient thermodynamic driving force for single-electron oxygen reduction to superoxide radicals, a critical reactive species in aerobic photocatalysis (Fig. 3d). Photoelectrochemical characterization revealed distinct charge transfer behaviours. Transient photocurrent responses (Fig. 3e) demonstrated reduced current densities for Pd-incorporated COFs, while electrochemical impedance spectroscopy (EIS) showed increased semicircle radii (Fig. 3f), correlating with higher charge-transfer resistance.

Imines are essential intermediates in the synthesis of biologically active compounds, including pharmaceuticals and natural products, where they frequently appear as key structural motifs. Examples include their role as intermediates in the synthesis of berberine alkaloids and etofenprox insecticides. As a result, the rapid oxidative coupling of benzylamines to access these functionally diverse imines is a methodologically significant approach. The photocatalytic performance of the Por-Pd/bpy-COF and the Por-bpy-COF was evaluated for the oxidative coupling of benzylamines to *N*-benzylidenebenzylamines under visible light irradiation ($\lambda > 400$ nm, 30 mW cm^{-2}). Both COFs exhibited rapid reaction kinetics, achieving >98% conversion within 60 min (Table S3, ESI†), with activity strictly contingent upon simultaneous light irradiation and O_2 saturation (entries 1 and 5, Table S3, ESI†). Control experiments established the indispensability of each component: no conversion (<2%) occurred under dark conditions or without a catalyst; anaerobic reactions under a N_2 atmosphere yielded <5% conversion, confirming O_2 as the terminal oxidant (entries 2–4, Table S3, ESI†). Experiments conducted under air conditions demonstrated conversions exceeding 62% for both catalysts (entries 7 and 8, Table S3, ESI†).

Reactive oxygen species[24,25] (ROS) quenching experiments employing *p*-benzoquinone ($O_2^{\bullet-}$ scavenger) and potassium iodide (h^+ scavenger) suppressed conversion to 19.8% (*vs.* 98% control), implicating $O_2^{\bullet-}$ radicals and hole-mediated oxidation as dominant pathways (entries 9–14, Table S3, ESI†). To decouple the roles of porphyrin and bipyridine motifs, we evaluated the TAPT-bpy-COF (a porphyrin-free analogue [entry 6, Table S3, ESI†]), which exhibited negligible activity (2.5% conversion), underscoring the critical role of porphyrin-centered excited states in photoredox cycles.[26]

Substrate scope evaluation (Table 1) demonstrated broad functional group tolerance. As shown in Table 1, good conversion was achieved in most cases. The effect of substituents on the conversion and selectivity was investigated compared to the background reaction. Electron-rich substrates (*e.g.*, 4-methylbenzylamine, entry 2 in Table 1) achieved >95% conversion with >90% selectivity. The sterically hindered analogue (2-methoxybenzylamine, entry 8 in Table 1) showed reduced activity (90% conversion), while strongly electron-deficient derivatives (4-nitrobenzylamine, entry 7 in Table 1) were largely inert (22.7%). Heterocyclic amines, such as (thiophen-2-yl)methanamine (entry 10 in Table 1), retained high efficiency (98% conversion and 96% selectivity in 60 min), highlighting the COFs' compatibility with π-conjugated systems.

The presence of $O_2^{\bullet-}$ was further verified by electron paramagnetic resonance (EPR) spectroscopy (Fig. S5, ESI†), in which $O_2^{\bullet-}$ excitation signals were recorded for the Por-bpy-COF (Fig. S5a, ESI†) and the Por-Pd/bpy-COF (Fig. S5b, ESI†). The gradual enhancement of the $O_2^{\bullet-}$ signal with time since the onset of illumination suggests that $O_2^{\bullet-}$ can be generated in the Por-bpy-COF and the Por-Pd/bpy-COF by excitation in the presence of light. The gradual enhancement of the $O_2^{\bullet-}$ signal captured by 5,5-dimethyl-1-pyrrolinoline N-oxide (DMPO) with time again supports the presence of $O_2^{\bullet-}$ generated during the reaction. Based on these experimental findings, a plausible mechanism is proposed to explain the aerobic oxidative coupling process of benzylamine by the Por-Pd/bpy-COF photocatalyst.

Subsequently, the recyclability of the Por-Pd/bpy-COF and the Por-bpy-COF was systematically evaluated under identical conditions. Following each oxidative coupling reaction, both catalysts were recovered *via* filtration, washed with acetonitrile, and directly reused for subsequent cycles. As depicted in Fig. S6 and S7 (ESI†), the Por-Pd/bpy-COF exhibited exceptional stability, maintaining a conversion efficiency exceeding 95% across five consecutive runs. In contrast, the Por-bpy-COF experienced a 13% decline in catalytic activity under identical recycling

Table 1 Light-induced oxidative coupling of benzylamines over the Por-Pd/bpy-COF[a]

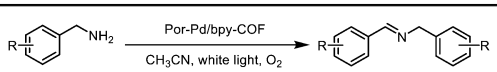

Entry	Substrate	Product	t (min)	Conv.[b] (%)	Sel.[b] (%)
1		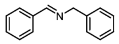	60	98.6	99
2	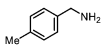	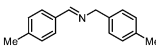	60	98.8	99
3	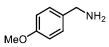	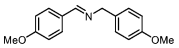	60	92.7	92
4	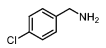	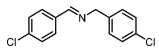	45	91.2	80
5	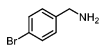	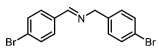	45	93.5	71
6	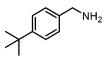	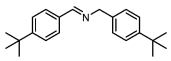	60	94.8	92
7	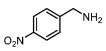	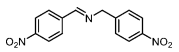	60	22.7	92[c]
8		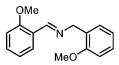	45	90.5	83
9		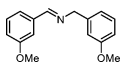	45	87.7	84
10		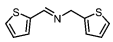	60	98.2	96

[a] Reaction conditions: amine (0.4 mmol), Por-Pd/bpy-COF (5 mg), MeCN (1 mL), white light, O_2 (1 atm), room temperature. [b] Determined by GC-FID using chlorobenzene as the internal standard, conversion of primary amines, and selectivity of imines. [c] Calculated from the obtained isolated yield.

conditions, highlighting the critical role of palladium incorporation in enhancing framework resilience during redox cycling. The recovered catalysts were characterized, and the Por-Pd/bpy-COF catalysts maintained their original state before the experiment, as shown in Fig. S8–S10 of the ESI.† The hot filtration test of the Por-Pd/bpy-COF in the benzylamine oxidative coupling reaction demonstrated the stability of the catalysts, as illustrated in Fig. S11 of the ESI.†

Experimental evidence supports the proposed mechanism (Fig. 4) for the light-driven aerobic oxidative coupling of benzylamine catalyzed by the Por-Pd/bpy-COF. Photoexcitation of the catalyst under white light irradiation generates electron–hole pairs, whereupon photogenerated holes oxidize benzylamine to form radical cation intermediates. Concurrently, electrons are transferred to molecular oxygen, yielding superoxide radicals ($O_2^{\bullet-}$). The $O_2^{\bullet-}$ species subsequently combines with hydrogen atoms from benzylamine radical cations, producing benzaldimine along with hydrogen peroxide as a by-product. Finally, nucleophilic attraction by a second benzylamine molecule on the benzaldimine intermediate affords the target product *N*-benzylbenzaldimine.

In conclusion, the design and synthesis of the Por-bpy-COF and the Por-Pd/bpy-COF highlight the potential of porphyrin-based COFs as efficient visible-light photocatalysts. Their ordered porous structures and visible-light-harvesting porphyrin units synergistically contribute to high catalytic performance in benzylamine oxidative coupling, achieving consistent

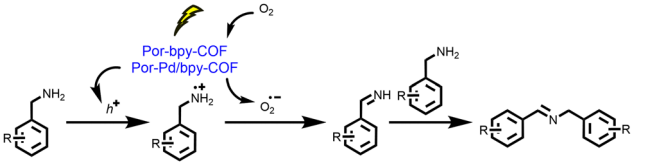

Fig. 4 A proposed mechanism of the aerobic oxidation of benzylamine to *N*-benzylbenzaldimine by COF photocatalysis.

conversion and selectivity across various substrates. The incorporation of Pd in the Por-Pd/bpy-COF enhances charge separation while retaining the COFs' intrinsic advantages, and robust stability, confirmed through post-reaction analyses, further validates their practical applicability. This study provides a framework for engineering porphyrin-COFs with tailored functionalities, advancing sustainable photocatalysis and offering insights for the development of energy-efficient platforms for organic transformations.

This work was supported by the State Key Laboratory of Chemical Oncogenomics and the Basic and Applied Basic Research Foundation of Guangdong Province (2025A1515011980).

Conflicts of interest

The authors declare no conflicts of interest.

Data availability

The data underlying this study are available in the published article and its ESI.†

References

1 J. Ran, *et al.*, *Chem. Soc. Rev.*, 2014, **43**, 7787.
2 Z. Wang, C. Li and K. Domen, *Chem. Soc. Rev.*, 2019, **48**, 2109.
3 D. M. Schultz and T. P. Yoon, *Science*, 2014, **343**, 1239176.
4 K. E. Dalle, *et al.*, *Chem. Rev.*, 2019, **119**, 2752.
5 T. Li, *et al.*, *J. Mater. Sci. Technol.*, 2024, **169**, 82.
6 B. Zhu, *et al.*, *Adv. Mater.*, 2024, **36**, 2310600.
7 A. Kharazmi, *et al.*, *RSC Adv.*, 2025, **15**, 1081.
8 K. Geng, *et al.*, *Chem. Rev.*, 2020, **120**, 8814.
9 A. Rodriguez-Camargo, K. Endo and B. V. Lotsch, *Angew. Chem., Int. Ed.*, 2024, **63**, e202413096.
10 B. Mishra, *et al.*, *Adv. Mater.*, 2024, 2413118.
11 P. J. Waller, F. Gándara and O. M. Yaghi, *Acc. Chem. Res.*, 2015, **48**, 3053.
12 J. M. Lee and A. I. Cooper, *Chem. Rev.*, 2020, **120**, 2171.
13 C. A. Trickett, *et al.*, *Nat. Rev. Mater.*, 2017, **2**, 17045.
14 H. Wang, *et al.*, *Chem. Soc. Rev.*, 2020, **49**, 4135.
15 H. Hu, *et al.*, *Chin. J. Catal.*, 2018, **39**, 1167.
16 A. Lopez-Magano, *et al.*, *Adv. Mater.*, 2023, **35**, 2209475.
17 C. Xu, *et al.*, *Chem. Sci.*, 2018, **9**, 3152.
18 P. Bai, *et al.*, *Catal. Sci. Technol.*, 2019, **9**, 5803.
19 C.-P. Dong, *et al.*, *ACS Omega*, 2016, **1**, 799.
20 Y.-N. Gong, *et al.*, *J. Am. Chem. Soc.*, 2020, **142**, 16723.
21 G. Lin, *et al.*, *J. Am. Chem. Soc.*, 2017, **139**, 8705.
22 M. Lu, *et al.*, *Angew. Chem., Int. Ed.*, 2019, **58**, 12392.
23 Y. Qian, *et al.*, *J. Am. Chem. Soc.*, 2020, **142**, 20763.
24 W. Fang, *et al.*, *Anal. Methods*, 2018, **10**, 2205.
25 P. Wu, *et al.*, *ACS Appl. Mater. Interfaces*, 2017, **9**, 10512.
26 H. Chen, *et al.*, *J. Phys. Chem. C*, 2023, **127**, 14137.